# X-ray focusing below 3 nm with aberration-corrected multilayer Laue lenses

J. Lukas Dresselhaus,[1] Margarita Zakharova,[2] Nikolay Ivanov,[2] Holger Fleckenstein,[2] Mauro Prasciolu,[2] Oleksandr Yefanov,[2] Chufeng Li,[2] Wenhui Zhang,[2] Philipp Middendorf,[2] Dmitry Egorov,[2] Ivan De Gennaro Aquino,[2] Henry N. Chapman,[1,2,3,4] and Saša Bajt[1,2,*]

[1]*The Hamburg Centre for Ultrafast Imaging, Universität Hamburg, Luruper Chaussee 149, 22761 Hamburg, Germany*
[2]*Center for Free-Electron Laser Science CFEL, Deutsches Elektronen-Synchrotron DESY, Notkestr. 85, 22607, Hamburg, Germany*
[3]*Department of Physics and Astronomy, Uppsala University, Box 516, Uppsala SE-75120, Sweden*
[4]*Department of Physics, Universität Hamburg, Luruper Chaussee 149, 22761 Hamburg, Germany*
[*]*sasa.bajt@desy.de*

**Abstract:** Multilayer Laue lenses are volume diffractive optical elements for hard X-rays with the potential to focus beams to sizes as small as 1 nm. This ability is limited by the precision of the manufacturing process, whereby systematic errors that arise during fabrication contribute to wavefront aberrations even after calibration of the deposition process based on wavefront metrology. Such aberrations can be compensated by using a phase plate. However, current high numerical aperture (NA) lenses for nanometer resolution exhibit errors that exceed those that can be corrected by a single phase plate. To address this, we accumulate a large wavefront correction by propagation through a linear array of 3D-printed phase correcting elements. With such a compound refractive corrector (CRC), we report on a point spread function with a full-width at half maximum area of $2.9 \times 2.8$ nm$^2$ at a photon energy of 17.5 keV.

## 1. Introduction

Hard X-rays are well suited for high-resolution imaging of thick materials and objects due to their short wavelength and high penetration power. Ultra-low emittance storage rings (4th generation synchrotrons) provide extremely brilliant X-rays, which, combined with high precision optics, enable diffraction limited imaging of such objects especially by scanned-probe methods such as fluorescence imaging or ptychography [1]. Triggered by the development of these sources there are worldwide efforts to develop better and more precise optics [2]. The achievable spatial resolution in an X-ray microscope is proportional to the wavelength divided by the numerical aperture (NA, equal to $\sin\alpha$ for a full convergence angle $2\alpha$ of the objective lens). Thus, highest resolution imaging in a microscope requires a lens of largest possible NA. However, the very same weak interaction that make X-rays attractive for imaging also makes them difficult to focus. The critical angle of reflection quantifies the ability to bend X-rays in a given interaction. Equal to $\sqrt{2\delta}$ for a refractive index $n = 1 - \delta + i\beta$, the critical angle of reflection for 10 keV photons from gold is 7.7 mrad, for example, and diminishes with decreasing wavelength. This limiting angle also applies to classes of refractive lenses [3, 4]. X-ray deflection angles can be extended by increasing the interactions between light and matter as by the multitude of reflections in a whispering gallery reflector [5, 6], or by dynamical diffraction in a crystal or multilayer mirror [6]. In the latter case, high scattering angles are achieved in proportion to the spatial frequency component in a structure, but useful efficiency at hard X-ray wavelengths still relies upon multiple scattering. High-NA hard-X-ray diffractive optics thus require periods comparable to the imaging resolution (nanometers) in a lens structure as thick in the direction of beam propagation as half the Pendellösung length (several micrometers) [7]. Such lenses, with layered structures of

nanometer thickness and an aspect ratio of many thousands, can be prepared by layer deposition and are referred to as multilayer Laue lenses (MLLs) [7].

To achieve diffraction-limited focusing performance in a diffractive lens, the thickness and position of any layer pair must be precise to a fraction of its period. Any misplacement leads to a wavefront aberration. It is extremely difficult to achieve this requirement. For example, a lens of 100 µm height with a smallest layer period of 2 nm would require a deposition process with a relative precision much better than $10^{-4}$ [8]. A source of error in the fabrication of MLLs is the stability of the deposition process, and in particular the change in deposition rates over days-long periods it takes to deposit the full structure. As long as this process is reproducible, it can be calibrated by determining the errors induced in the layer periods, which can be obtained simply from a measurement of the wavefront error of the lens. After such a feedback, the high-NA lenses produced today still have residual wavefront errors of several waves peak to valley and hence are far from the diffraction-limited performance needed for focusing down to 1 nm. A viable approach to achieve that goal is to compensate wavefront aberrations using a refractive phase plate [9–15], as long as the magnitude of the error is within bounds that can be recreated in a refractive structure. The correction requires first measuring the aberration and then fabricating an appropriate phase plate to match. The accuracy of the resulting wavefront then depends on the accuracy of the measurement and of the ability to fabricate a structure with the equal but opposite phase deviation. Of course, only the lens carries the burden of strong focusing and the refractive phase plate only need address the residual wavefront. Given that a wavelength $\lambda$ of phase is induced by a thickness $t = \lambda/\delta$, the required precision on the thickness variation of the plate is micrometers, compared with the nanometer precision required of the MLL structure. As is the case for refractive lenses, materials should be chosen that maximize the phase shift for a given transmission loss due to absorption. This favors materials of high ratio $\delta/\beta$, which for X-rays in the range of about 10 keV to 30 keV are of low atomic number [16].

Refractive phase plates can be made either by subtractive or additive processes, such as laser ablation machining or 3D printing [17]—both of which allow for fast and precise fabrication [18, 19]. Printed structures are usually made of a polymer, consisting of elements of suitably low atomic number. Nevertheless, the refractive decrement $\delta$ is of the order of $10^{-6}$ and hence thickness ranges of hundreds of micrometers are needed. For example, to correct a peak-to-valley aberration of 5 waves at 17.5 keV, a thickness variation of about 400 µm is required in a polymer structure. For a lens that is 40 µm high, the resulting structure has a high aspect ratio that we find is usually structurally very unstable. To reduce this aspect ratio and to relax printing specifications, we have found that it is better to distribute the correction over several correcting elements. These structures are more stable and more easily printed. A phase plate consisting of several identical elements printed in a row, which we refer to as a compound refractive corrector (CRC) [13], has been used successfully to compensate the aberrations of a single MLL to give a wavefront with an RMS error reduced by more than 80 % [20]. Here, we present results achieved with high NA (NA = 0.014) MLLs. Without correction, these lenses could focus X-rays to a spot size below 5 nm, and obtained a Strehl ratio of 0.018. By introducing a CRC in the beam path, we corrected most of the residual aberrations and substantially improved the imaging performance with a Strehl ratio of 0.086. In the following, we first describe the development cycle to produce high-NA MLLs, utilizing a laboratory X-ray source for wavefront characterization. This is followed by a description of the design and fabrication of CRCs that were used in this work, generated based on the measurements made with the laboratory source. Using synchrotron radiation, the wavefront errors and point spread functions (PSF) of a lens pair were measured with and without the CRC. Finally, the wavefront aberration contributions were decomposed into a set of orthogonal functions (derived from Zernike polynomials) to determine which contributions were most readily corrected.

## 2. Fabrication and characterization of multilayer Laue lenses

MLL structures are built of alternating layers of at least two materials to form each period. The thicknesses of these periods decrease approximately inversely with the distance from the optical axis, following the same dependence of periods in a Fresnel zone plate that gives an extra wave of path per period for rays directed to the focus. MLLs are usually created by deposition onto a flat substrate (such as a Si wafer) by magnetron sputtering, which has the stability and controllability to produce structures of tens of thousands of nanometer-thick layers. Using a focused ion-beam instrument, a lens is sliced and removed from this multilayer stack to be used in a transmission geometry. The thickness of this slice in the direction of beam propagation is chosen to maximize the Laue diffraction efficiency and is equal to half the pendellosung period as noted above. This is the propagation distance through a thickness of a periodic structure (or crystal) where the transfer of energy from the undiffracted beam to the diffracted beam is greatest, and depends on the optical properties of the multilayer materials, the ratio of their thicknesses, and the X-ray wavelength. The structure is usually designed as an off-axis lens in order to limit the largest deposited period. The NA of the lens depends on the difference of the maximum and minimum scattering angles, which is ultimately limited by the smallest period in the structure, located furthest from the optical axis. High efficiency is only achieved over a limited range of incident angles (the Darwin width or rocking-curve width) which decreases as the period decreases and for high-NA lenses is narrower than the NA of the lens itself. Therefore, for focusing an incident collimated beam, the layers must vary in their tilt to ensure that the Bragg condition is satisfied for each position in the lens. For this, the layers lay normal to a cylinder with a radius of twice the focal length, and achieved by shadowing the source [21] or the substrate [22] in the deposition process. Since the layers are deposited onto a flat substrate, the resulting lens only focuses in one dimension, analogous to a cylindrical lens. Two lenses, oriented to focus in orthogonal directions and separated by a distance equal to the difference of their focal lengths, create a two-dimensional focus in a comparable way to Kirkpatrick-Baez mirrors. A feature of orthogonally-oriented MLLs is that the wavefront aberration map is separable into functions of the two orthogonal directions due to the contributions of each lens. A corollary to this is that if the wavefront is not separable then the lenses are not perfectly orthogonal [23].

The MLLs used in this work were fabricated by the alternating deposition of silicon carbide (SiC) and tungsten carbide (WC). These materials remain amorphous over the full range of used periods [24] and form very sharp and smooth interfaces even for periods as low as a few nanometers [25]. The resulting multilayer structures have high thermal stability [26]. The lenses produced for this work were both cut from a multilayer structure consisting of 10 854 periods deposited onto a flat wafer in a single deposition run. The wafer was shadowed in two different regions by straight-edge masks [22] that were placed 1400 µm and 1210 µm above the substrate, allowing two lenses to be cut with different focal lengths (1.15 mm and 1.25 mm) and optimized for a common photon energy (of 17.5 keV). Due to the scaling of the multilayer in the shadowed regions and since the gradient of the profile must intersect the optical axis at a point twice the (diffractive) focal length away, the lens of shorter focal length was cut from the shadow with the broader penumbral width and vice versa [27]. The short focal length lens had a height of 34 µm, NA = 0.015, and was used as the vertically-focusing lens (vMLL) while the horizontally-focusing lens (hMLL) was of 35 µm height, NA = 0.014. The lenses were designed to be off axis with the largest periods starting at a distance of 10 µm from the optical axis. This geometry allows the zero-order (non-focused) beam transmitted through the lenses to be blocked by an L-shaped blade located a distance of 261 µm from the focus, setting the working distance. Both lenses were cut to a thickness of 7 µm for optimum focusing efficiency.

In the hard-X-ray regime, wavefront aberrations can be measured by a variety of interferometric and non-interferometric methods [28–36]. For lenses of high NA we find that the non-interferometric method of ptychographic speckle tracking is particularly suitable [37–39]. An

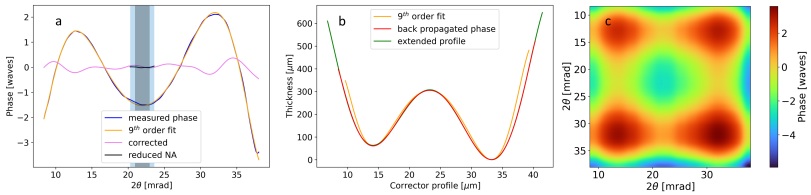


Fig. 1. (a) Wavefront of the vMLL lens as derived by robust ptychographic speckle tracking [40] (blue). A 9th order polynomial fit reduces local variations and high frequency noise (orange). The gray bar shows a typical angular span of CRLs with an NA of $10^{-3}$ and the blue bar shows the NA of a prior result of an MLL corrected with a phase plate [14]. The black line indicates the wavefront of our vMLL after subtracting trivial terms and stopping it down to the same NA as the MLL indicated by the blue bar. The violet line indicates the corrected wavefront as determined from the 2D wavefront (see Sec. 4). (b) The required corrector thickness based on the smoothed wavefront from (a) (orange), and numerically propagated 20 mm backwards using geometric ray tracing (red). An extension of the propagated profile (red) by 2 µm on each side to remove possible edge effects is shown in green. The horizontal axis shows the distance from the optical axis. (c) Uncorrected 2D phasemap $\phi(\mathbf{r}) = \phi_h(x) + \phi_v(y)$ expected assuming perfect orthogonal alignment.

object is placed in the converging or diverging beam out of the focus to form a highly magnified projection image on a far-field pixel-array detector. Residual aberrations cause distortions in this image, which can be revealed by moving the object in steps considerably smaller than the width of the defocused beam. The displacements of features as the object is stepped can be used to map out the phase gradient of the wavefront, without requiring prior knowledge of the object's structure. This method was recently extended with the addition of two machine learning techniques, Huber regression and non-parametric regression [40]. We employed this approach, referred to as robust ptychographic speckle tracking (RPST), as part of an iterative process to fabricate high-NA MLLs. A single lens cut from the multilayer created in a deposition run was characterized using our laboratory setup. The resulting wavefront was then used to update the deposition recipe, to account for reproducible systematic errors in the deposition run. We have qualified the laboratory metrology system by comparing results with those obtained using synchrotron radiation [20].

RPST measurements with the laboratory source were carried out on single MLLs focusing only in one direction. Measurements here were made using Mo K$\alpha$ emission at a photon energy of 17.5 keV. The procedure for testing a lens was as follows: The operating photon energy of the lens was first tested by a rocking scan [27] measured with the pixel array detector (Lambda, X-Spectrum) positioned about 0.3 m downstream. If this indicated that the operating energy does not match the testing energy of 17.5 keV then a new lens was cut from an adjusted position in the shadow profile of the deposited wafer. The lens focuses to a line focus which then diverges in one direction onto the detector. A transmission barcode-like sample, cut from a multilayer structure with layers of random thicknesses between 180 nm and 1000 nm was placed about 80 µm downstream of the line focus where the beam size had expanded to about 2.4 µm. This produces a one-dimensional projection image on the detector with a magnification of 25 000 at a distance of 2 m. Using a dwell time of 30 s per point the sample was scanned with a step size of 100 nm over a total distance of 10 µm in about 50 minutes. The wavefront $\phi_v$ of the vMLL lens obtained by tracking features of the barcode sample using RPST is plotted in Fig. 1 (a) as a function of the scattering angle $2\theta$, proportional to position $y$ in the lens aperture. The convention used here is that lower phase lags behind higher. Having been cut from the same multilayer structure, the wavefront $\phi_h$ of the hMLL lens was very similar and not shown here.

The wavefront of the beam focused by the pair of lenses was not measured in the laboratory since the diverging beam is spread over many hundred times more detector pixels than for a single lens, requiring exposure times that are prohibitively long. This 2D wavefront can be computed from the sum of phases as $\phi(\mathbf{r}) = \phi_h(x) + \phi_v(y)$ (see Fig. 1 (c)), assuming they are oriented orthogonally and separated appropriately to focus to a common plane. The 2D wavefront of the pair was measured at the synchrotron as described below, but only after the phase plate had been prepared.

We have previously noted that a linear drift of the deposition rate during lens fabrication causes a third-order wavefront aberration [8]. The initial deposition in the development cycle produced a lens with a wavefront error of 4.25 waves, RMS, dominated by this third-order term. As long as the deposition process is reproducible, the drift can be calibrated by using the wavefront measurement. Having access to the laboratory setup considerably accelerates this development cycle, by adjusting the deposition recipe according to the measured aberration. The lenses created here followed such a process which ultimately yielded the wavefront of Fig. 1 (a). The RMS wavefront error was 1.36 waves after removing piston, tilt and defocus and was dominated by the fourth-order term, which causes spherical aberration. This wavefront certainly limits the optical performance of the MLL, but this is still an outstanding result given the size of the lens NA and the fact that aberrations grow with a high power of the NA (to the fourth power in this case). It is therefore instructive to compare it with the aberrations of other state-of-the-art X-ray optical elements. The gray bar in 1 (a) indicates the typical angular range of a CRL at similar photon energy ($10^{-3}$) while the blue bar shows the angular range of an MLL prepared by another group with an NA of 0.0016 [14], which is 12 % of that of the lens used here. The wavefront of our lens, apertured by this reduced NA and after subtracting piston, tilt and defocus, is shown as the black line in Fig. 1 (a). Over that NA, our MLL has an RMS wavefront of only 0.002 waves, which is smaller than the Marechel criterion [41], meaning that it would exhibit diffraction limited focusing without further correction. With an NA over 8 times larger than this, it is considerably harder to control the deposition process to achieve similar results for the full lens. Phase correction is thus necessary for high-NA lenses.

## 3. Design and fabrication of the compound refractive corrector

The desired phase correction $\phi_c(\mathbf{r})$ generated by the phase corrector is simply the negative of the wavefront aberration $\phi(\mathbf{r})$ of the MLL, determined as a function of the position vector $\mathbf{r}$. For a material of refractive index $n = 1 - \delta$, this can be achieved by shaping the thickness according to

$$t(\mathbf{r}) = -\frac{\lambda}{2\pi\delta}\phi_c(\mathbf{r}). \tag{1}$$

The negative sign is due to the fact that the refractive index of the material is less than unity and so the phase actually advances in the structure, relative to vacuum. In this work the phase corrector was produced by three-dimensional (3D) printing by two-photon polymerisation. The resulting polymer structure with the composition $C_{14}H_{18}O_7$ and density of $1.2\,\mathrm{g\,cm^{-3}}$ is calculated to have a refractive index decrement of $\delta = 8.62 \times 10^{-7}$ at 17.5 keV [42]. The 5.5 wave peak-to-valley aberration of the vMLL lens seen in Fig. 1 (a) would therefore need a total variation of thickness of $5.5\lambda/\delta = 450\,\mu\mathrm{m}$ as shown in Fig. 1 (b). The desired correction was computed by first smoothing the measured wavefront profiles $\phi_h(x)$ and $\phi_v(y)$ by fitting ninth-order polynomials to them. Given that the MLLs have heights of 34 µm and 35 µm, it is apparent that the phase plate would consist of high aspect-ratio structures that we find are structurally unstable as discussed further in Sec. 5. By dividing the corrector into $N$ identical structures, the thickness profile of each is $t(\mathbf{r})/N$.

When using MLLs to focus a collimated beam, the phase correction is best placed upstream of the lens and ideally placed as close as possible to it. In practice, due to the instrumentation

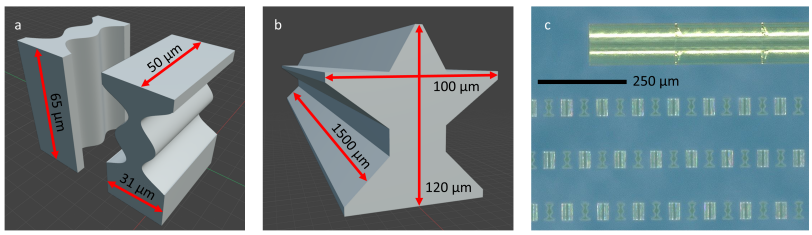


Fig. 2. (a) A pair of 1D CRC elements, one correcting 1/20 of aberrations in the vertical and the other 1/20 of aberrations in the horizontal direction. 20 identical pairs were printed in a row to form a full CRC. (b) Alignment structure used to aid the positioning of the CRC. Two such structures were printed about 9.5 mm apart to increase the angular sensitivity. (c) Optical microscope image of the printed structures. In addition to the CRC with 20 element pairs, additional ones with more and fewer elements were printed onto the same substrate. The image shows three rows of CRCs together with an alignment structure at the top.

to hold and orient the two lenses as well as the phase plate, the distance between the phase plate and lens was about 20 mm. This is far enough away that the structure must be modified to account for the evolution of the wavefront due to propagation to the lenses, but close enough that the phase does not manifest as a large change in beam intensity. The thickness profile $t(\mathbf{r})$ was therefore modified by numerically propagating the wavefront backwards by 20 mm by geometric ray tracing. The corrected thickness profile in the vertical direction is shown in red in Fig. 1 (b). This profile was extrapolated beyond the edges by 2 µm on both sides to avoid large phase gradients which cause large changes in beam intensity. For these computations we assume that the corrector is a thin plate (even for the compound corrector).

The CRC was printed with a Photonic Professional GT printer (Nanoscribe) via two-photon polymerization [43]. Printing was done with a 25× objective and IP-S resist, giving a theoretical printing resolution of 595 nm × 595 nm × 3313 nm [44,45] in the $x$, $z$, and $y$ directions (see Fig. 3 for the coordinate system). The orientation of the printed structure was such that the optical axis is parallel to the glass substrate and that the substrate is horizontal in use. Thus, the correction profile for the vMLL lens varies in the direction normal to the substrate (the direction of the slowest step in the 3D print raster and worst print resolution) and that of the hMLL varies parallel to the print substrate. We found that printing structures with thicknesses that vary in both the $x$ and $y$ directions tended to create rough and distorted surfaces, even for a range of print speeds and doses. These errors and surface irregularities could largely be avoided, however, when printing structures that only varied as a function of $x$ or $y$. Thus, we separated the compound corrector into elements that corrected these individual components (and hence the lenses), as shown in Fig. 4 (a). The required total correction thickness profiles $t(x)$ and $t(y)$ were both divided into $N = 20$ identical elements with mirrored faces as shown in Fig. 2 (a). The profile of each face is thus $t(x)/(2N)$, for example. The minimum thickness of each element was set to 6 µm to provide stable structures, adding total uniform thickness of polymer of 240 µm. The horizontally and vertically correcting structures were interleaved in the compound structure and the distance between the elements was 20 µm, producing a corrector with a total length of about 2 mm. The optical path through the polymer ranged from 240 µm to 1200 µm, giving a minimum calculated transmittance of 96.4 % at 17.5 keV photon energy.

To further increase the structural stability and to avoid printing sharp edges, 5 µm thick sidewalls were included in the design of the horizontally correcting structure. For the vertically correcting element, a similar structure was added to the top and the whole structure was placed on a 20 µm thick pedestal as illustrated in Fig. 2 (a). Because of its long length, even a small

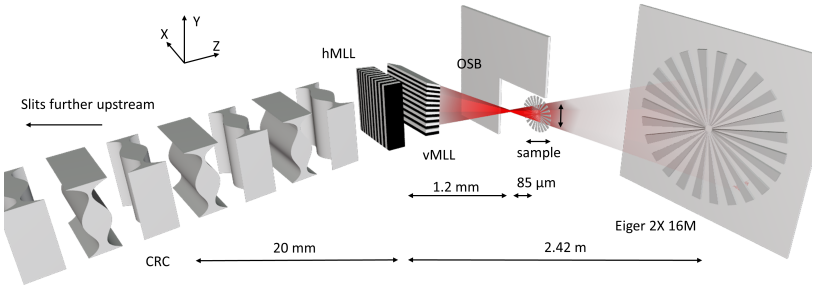


Fig. 3. Sketch of the experimental setup used at the synchrotron beamline. The CRC was positioned upstream of the MLLs. A sample, which was placed slightly downstream from the focus, was scanned and magnified images were recorded on an Eiger detector. An order sorting blade placed between the lenses and the focus blocked undiffracted beams. Upstream slits (not shown) were used to reduce the beam size to match the size of the lenses.

rotational misalignment has a large effect on its performance. To simplify the alignment, two alignment structures (Fig. 2 (b)) were printed at the start and at the end of the substrate, outside the beam path of the lenses.

The CRC and guiding structures were printed on a 20 mm × 10 mm rectangular ITO-coated glass substrate, 0.7 mm thick. Seven CRCs with different numbers of elements were printed on the same substrate, which allowed tuning the correction by a relative factor of up to ± 10 %. The 3D printing was performed with a slicing distance of 0.4 µm, a hatching distance of 0.4 µm with a contour count of 5 and a contour distance of 0.4 µm. Alignment structures, which do not require smooth surfaces, were printed with high dose (100 % laser power and a speed of 40 000 µm $s^{-1}$) while the CRCs, which require precise printing, were printed with low dose (50 % laser power and a speed of 100 000 µm $s^{-1}$). The printed structures were developed in PGMEA (propylene glycol methyl ether acetate) for 30 minutes and then immersed in isopropanol for 5 minutes. Finally, they were UV cured for 30 minutes to harden the structure. The time to print the seven CRCs and alignment structures was 7 hours. However, printing only a single CRC along with the alignment structures only takes 1.5 hours.

## 4. Results

The MLLs with and without CRCs were tested at the P11 beamline at PETRA III (Hamburg, Germany), using ptychographic speckle tracking to measure the wavefront aberrations of the lens pair. The lenses were mounted in a portable X-ray microscope setup. Each lens was mounted on a separate hexapod (SmarAct SMARPOD P-SLC-17), giving motion in all six degrees of freedom for fine alignment. The CRC with 20 pairs of elements was placed 20 mm upstream on a third hexapod. A pair of slits positioned about 300 mm upstream was used to match the beam size to the aperture of the MLLs. An L-shaped blade was placed between the lenses and the focus to block the direct (undiffracted) beam.

For the wavefront measurements, a gold Siemens star object, prepared by electron beam lithography on a silicon nitride substrate, was placed in the beam about 85 µm downstream of the focus (Fig. 3). It consisted of 24 spokes with a thickness of 500 nm and innermost spoke width of 10 nm. An Eiger 2X 16M (Dectris) detector, with a pixel size of 75 µm was placed 2.42 m downstream. At this distance, the magnification of the projection image of the Siemens star was 28 500. Given the NA's of the two lenses, the diverging beam covers an area of 68.3 mm × 71.3 mm on the detector, or 910 × 950 pixels. By the Fresnel scaling theorem [46], this image is equivalent to the in-line hologram of the object with a collimated beam, recorded at

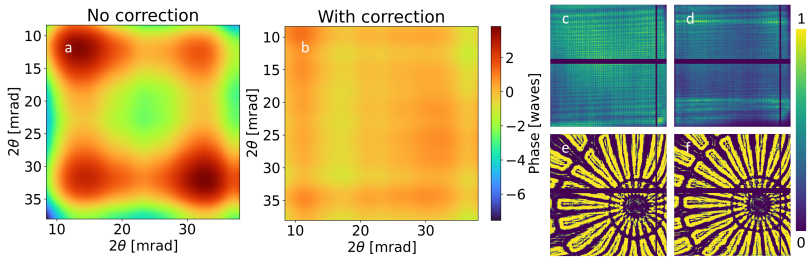


Fig. 4. Comparison of the 2D wavefronts without (a) and with (b) the CRC in the beam. The RMS is reduced from 1.67 waves to 0.40 waves. For both wavefronts, trivial terms such as piston, tilts and defocus are removed. White-field of the beam without (c) and with (d) CRC present. A single white-field corrected image of the sample without (e) and with (f) the CRC present.

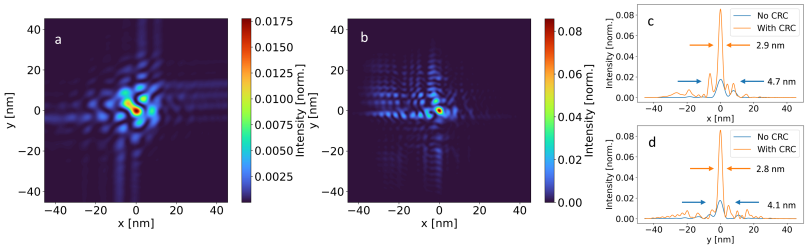


Fig. 5. Point spread function (PSF) of the lens pair without (a) and with (b) CRC, as obtained by propagating the white-fields and wavefronts shown in Fig. 4 to the focal plane. The intensity is normalized to a perfect lens pair of otherwise equal dimensions. CRC implementation reduced the focus spot size from 4.7 nm × 4.1 nm to 2.9 nm × 2.8 nm FWHM. Line cuts through the PSFs shown in (a) and (b), along the vertical (c) and horizontal (d) directions.

a distance of about 85 µm on a detector with 2.6 nm pixels. The intensity distribution without the object, which we refer to as the white-field image, can be divided from the projection image such as shown in Figs. 4 (e) and (f). Speckle-tracking measurements were performed by scanning the sample on a 6 × 6 grid of points with a step size of 0.2 µm, a field size of 1 µm × 1 µm and an exposure time of 1.5 s for a total scan time of about 1 minute. The region of interest of each detector frame was cropped to the region of the bright-field projection image. These frames were processed by the RPST software in a similar fashion as described above.

Figure 4 shows the comparison of the measured wavefronts without (a) and with (b) the CRC in the beam, after subtracting piston, tilt, and focus. The CRC reduced the wavefront aberrations from 1.67 to 0.40 waves (RMS). The white-field images obtained without and with the CRC in the beam are depicted in Fig. 4 (c) and (d), respectively. A slight intensity redistribution is observed. This can be explained by the transport of intensity of the incident beam from the CRC structure to the plane of the lenses whereby the gradient of the phase gives rise to a redistribution of intensity. The projection image of the Siemens star is clearly improved with the CRC, as can be seen in the reduction in distortions of the hologram in Fig. 4 (f) compared to that in Fig. 4 (e).

The complex-valued wavefront at the pupil of a lens completely specifies the coherent beam that propagates to the focus and beyond. This can be formed from the square root of the white-field intensity and the wavefront phase. Intensity distributions calculated by propagating this to the focal plane (by a Fourier transform) are shown in Figs. 5 (a) and (b) for the cases before and after adding the CRC. Plots along cuts in the horizontal and vertical directions through the most

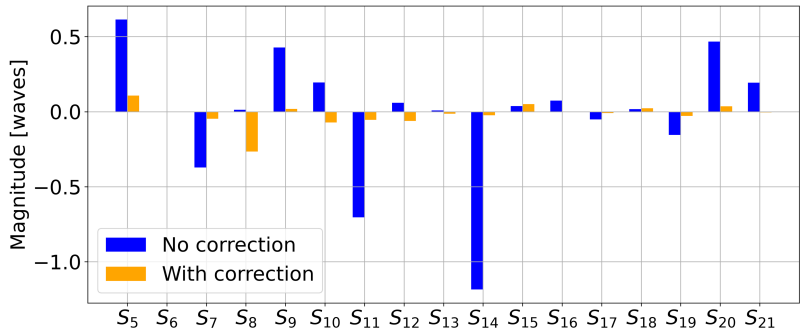


Fig. 6. Decompositions of the 2D wavefronts shown in Figs. 4 (a) and (b) into square Zernike-like polynomials, $S_k(x, y)$, following Noll's sequential indices. The magnitudes of the polynomials without the CRC are shown in blue while the ones with correction are shown in orange.

intense spot in the focus are are given in Figs. 5 (c) and (d), respectively. The area of the point spread function (PSF) was reduced from 4.7 nm × 4.1 nm to 2.9 nm × 2.8 nm when the CRC was introduced. The intensity profiles in Fig. 5 were all normalized to the peak intensity achievable with an aberration-free lens pair, and thus the peak values in the plots are equal to the Strehl ratio, which increased by a factor of 4.8 from 0.018 to 0.086.

To determine which wavefront contributions were reduced by the CRC, the wavefronts were decomposed into sums of Zernike-based polynomials $S_k(x, y)$ that are orthonormal over the domain of the rectangular lens pupil [47, 48]. These polynomials were obtained by a Gram-Schmidt orthogonalisation of Zernike polynomials defined in the circle that circumscribes the rectangular domain, and which follow Noll's indexing convention [49]. The first 21 terms of the decompositions are plotted in Fig. 6, omitting piston, tilt, defocus, and 0-90° astigmatism. (This last term is proportional to the relative spacing of the two lenses.) Most terms are greatly reduced, in particular spherical aberration $S_{11}$ and tetrafoil aberration $S_{14}$. These are the terms that give the characteristic four peaks in Fig. 4 (a) and which are caused by the dominant fourth-order polynomial wavefront error of each lens. Interestingly, while the vertical coma $S_7$ was reduced, the horizontal coma $S_8$ increased. We hypothesize that this could be a scale error of the print in this direction. A reduction in 45° astigmatism $S_5$ is noticed as well and could be explained by slight rotation of the CRC around the optical axis correcting for an apparent non-orthogonality of the two lenses.

## 5. Discussion

Further investigation on the printing parameters is required to improve surface smoothness and to optimize structures that integrate the correction into two-dimensional profiles, rather than separating corrections for the two lenses into interleaving structures. Printing the structure such that the optical axis is normal to the substrate would better match the voxel resolution of the 3D printer [50, 51]. This was also tested as a single phase plate structure but resulted in producing a structure with an aspect ratio of $\sim 25:1$ with little connection to the substrate. Even with a lot of additional supporting structures, such a single element is vulnerable to even slight bending which would misshape the induced phase significantly. The nature of the aberration to be corrected caused the printed structure to be pointy at its edges, which we found difficult to print, for either of the orientations. In addition, high local aspect ratios may place surfaces below the critical angle of reflection for the incoming rays, especially if the corrector is misaligned or bent by small angles in the milliradian range. This would certainly have detrimental effects on the wavefront.

For these reasons, it was concluded that a compound structure is be easier to fabricate and more robust to align.

One has to consider that the correction of large wavefront errors with a phase plate may lead to redistribution of intensity at the lens, especially if the stand-off distance is as large as it was here. Otherwise, wavefront engineering approaches must be employed to control both the phase and amplitude of the incident beam [52, 53]. Small errors may occur due to the neglected phase propagation between individual elements. The distance between the CRC and the lenses (20 mm) is much larger than the length of the CRC (2 mm), but wave propagation simulations showed that this effect is smaller than the printing precision and therefore negligible in this case. The offsets used to increase the stability of the structures, as well as the gaps between the elements, slightly increase the absorption of the CRC and increase the effect of intensity redistribution.

Diamond is an attractive alternative material to polymer, with much higher refractive index but similar absorption per phase shift. This material can be cut by a laser cutter [54, 55] or plasma focused ion beam. However, these elements would have to be fabricated successively and aligned in a row afterwards, which adds to their complexity. No damage or deformation of the polymer structure was observed due to exposure to X-rays. It changed slightly in color from transparent white to transparent yellow, but no change in refractive power was observed for the duration of its use over several days at the synchrotron beamline.

## 6. Summary

Multilayer Laue lenses are a promising optical technology to reach nanometer focusing of X-rays. The high diffraction efficiency of the deposited multilayer structure enables rays to be deflected by relatively large angles for lenses of high enough NA to achieve this goal. The accuracy required for the deposited structure is severe, however, with a required relative precision for the deposition of about $10^{-4}$ [8]. A feasible strategy to reach the smallest focal spots is therefore to manufacture an MLL as accurately as achievable and then correct for the residual wavefront error using a refractive phase corrector. Since the corrector is not required to provide any focusing power, the precision required in the thickness profile of the element is of the order of micrometers, equal to the ratio of the allowable optical path error divided by $\delta$, the refractive index decrement.

Here, we demonstrated the use of a compound refractive corrector to compensate the 2D wavefront aberration of a crossed pair of multilayer Laue lenses with NA = 0.015 operating at 17.5 keV photon energy (0.071 nm wavelength). An aberration-free lens with these parameters would focus an X-ray beam to a spot of width 2.1 nm. The lenses were produced as part of an iterative development cycle that used laboratory-based at-wavelength X-ray wavefront measurements to calibrate the multilayer deposition procedure. This produced lenses with a peak-to-valley wavefront error of about 5 waves over the full aperture. The fast development cycle (of achieving a wavefront measurement within a day of performing the deposition) was made possible by the use of the laboratory source coupled with the non-interferometric wavefront sensing method of ptychographic speckle tracking, a method with low requirements on coherence and monochromaticity. The achievable wavefront error of the deposited MLL far exceeded the state of the art when considering the high NA of the lens, but was still considerably large in terms of achieving near diffraction-limited performance. Indeed, the wavefront was found to be too large to be corrected by a single-element refractive corrector. The high thickness gradients required could not be reliably made in a refractive structure by the method of two-photon polymerisation 3D printing. Instead, we created a compound refractive corrector (CRC) out of a series of elements that each had only a fraction of the thickness variation required for the full correction. The CRC designed for the MLLs presented in this study was achieved with 20 individual element pairs, where each pair consisted of structures that separately corrected the vertical and horizontal aberration components. The CRCs were fabricated by two-photon polymerisation 3D printing. The MLL pair combined with the CRC was tested using synchrotron radiation and achieved

a PSF of 2.9 nm × 2.8 nm FWHM. The low wavefront error also enabled high-magnification projection holograms to be recorded of a Siemens star sample.

**Funding.** This work is funded by the Cluster of Excellence "CUI: Advanced Imaging of Matter" of the Deutsche Forschungsgemeinschaft (DFG) – EXC 2056 – project ID 390715994.

**Acknowledgments.** We thank Sabrina Bolmer, Harumi Nakatsutsumi, Julia Maracke and Tjark Delmas for technical support. We acknowledge DESY (Hamburg, Germany), a member of the Helmholtz Association HGF, for the provision of experimental facilities. Parts of this research were carried out at PETRA III synchrotron facility. We thank Johanna Hakanpää (DESY) and her team for assistance in using beamline P11. Beamtime was allocated for Proposal No. I-20220442. This work is funded by the Cluster of Excellence "CUI: Advanced Imaging of Matter" of the Deutsche Forschungsgemeinschaft (DFG) – EXC 2056 – project ID 390715994.

**Disclosures.** The authors declare no conflicts of interest.

**Data availability.** Data underlying the results presented in this paper are not publicly available at this time but may be obtained from the authors upon reasonable request.

## References

1. C. G. Schroer, I. Agapov, W. Brefeld, R. Brinkmann, Y.-C. Chae, H.-C. Chao, M. Eriksson, J. Keil, X. Nuel Gavaldà, R. Röhlsberger, O. H. Seeck, M. Sprung, M. Tischer, R. Wanzenberg, and E. Weckert, "PETRA IV: the ultralow-emittance source project at DESY," J. Synchr. Rad. **25**, 1277–1290 (2018).
2. G. E. Ice, J. D. Budai, and J. W. Pang, "The race to x-ray microbeam and nanobeam science," Science **334**, 1234–1239 (2011).
3. B. Lengeler, C. Schroer, J. Tümmler, B. Benner, M. Richwin, A. Snigirev, I. Snigireva, and M. Drakopoulos, "Imaging by parabolic refractive lenses in the hard x-ray range," J. Synchr. Rad. **6**, 1153–1167 (1999).
4. C. Bergemann, H. Keymeulen, and J. Van der Veen, "Focusing x-ray beams to nanometer dimensions," Phys. Rev. Lett. **91**, 204801 (2003).
5. A. Vinogradov, I. V. Kozhevnikov, V. V. Pustovalov, and V. F. Kovalev, "Concave and revolving mirrors of the x-ray region. 1." Z. Tekh. Fiz. **55**, 244–250 (1985).
6. E. Spiller, "Soft x-ray optics," (Optica Publishing Group, 1990).
7. H. Yan, R. Conley, N. Bouet, and Y. S. Chu, "Hard x-ray nanofocusing by multilayer Laue lenses," J. Phys. D **47**, 263001 (2014).
8. H. N. Chapman and S. Bajt, "A ray-trace analysis of x-ray multilayer Laue lenses for nanometer focusing," J. Opt. **22**, 115610 (2020).
9. K. Sawhney, D. Laundy, V. Dhamgaye, and I. Pape, "Compensation of x-ray mirror shape-errors using refractive optics," Appl. Phys. Lett. **109**, 051904 (2016).
10. F. Seiboth, A. Schropp, M. Scholz, F. Wittwer, C. Rödel, M. Wünsche, T. Ullsperger, S. Nolte, J. Rahomäki, K. Parfeniukas, S. Giakoumidis, U. Vogt, U. Wagner, C. Rau, U. Boesenberg, J. Garrevoet, G. Falkenberg, E. Galtier, H. Ja Lee, B. Nagler, and C. Schroer, "Perfect x-ray focusing via fitting corrective glasses to aberrated optics," Nat. Comm. **8**, 14623 (2017).
11. D. Laundy, V. Dhamgaye, T. Moxham, and K. Sawhney, "Adaptable refractive correctors for x-ray optics," Optica **6**, 1484–1490 (2019).
12. V. Dhamgaye, D. Laundy, S. Baldock, T. Moxham, and K. Sawhney, "Correction of the X-ray wavefront from compound refractive lenses using 3D printed refractive structures," J. Synchr. Rad. **27**, 1518–1527 (2020).
13. K. T. Murray, "Wavefront aberrations of high numerical aperture x-ray optics," Ph.D. thesis, Universität Hamburg (2021).
14. F. Seiboth, A. Kubec, A. Schropp, S. Niese, P. Gawlitza, J. Garrevoet, V. Galbierz, S. Achilles, S. Patjens, M. E. Stuckelberger, C. David, and C. G. Schroer, "Rapid aberration correction for diffractive x-ray optics by additive manufacturing," Opt. Express **30**, 31519–31529 (2022).
15. B. Ji, S. Yue, L. Zhou, M. Li, and G. Chang, "Novel figuring method for a multilayer Laue lens," Opt. Express **30**, 46838–46848 (2022).
16. B. Yang, "Fresnel and refractive lenses for x-rays," Nucl. Instrum. Meth. Phys. Res. A **328**, 578–587 (1993).
17. F. Seiboth, D. Brückner, M. Kahnt, M. Lyubomirskiy, F. Wittwer, D. Dzhigaev, T. Ullsperger, S. Nolte, F. Koch, C. David, J. Garrevoet, G. Falkenberg, and C. G. Schroer, "Hard X-ray wavefront correction via refractive phase plates made by additive and subtractive fabrication techniques," J. Synchr. Rad. **27**, 1121–1130 (2020).
18. "Photonic Professional GT2 ," https://www.nanoscribe.com/en/products/photonic-professional-gt2/#tab-17290. Accessed: 2023-02-06.
19. A.-I. Bunea, N. del Castillo Iniesta, A. Droumpali, A. E. Wetzel, E. Engay, and R. Taboryski, "Micro 3D printing by two-photon polymerization: configurations and parameters for the nanoscribe system," in *Micro,* vol. 1 No.2 (MDPI, 2021), pp. 164–180.

20. J. L. Dresselhaus, H. Fleckenstein, M. Domaracký, M. Prasciolu, N. Ivanov, J. Carnis, K. T. Murray, A. J. Morgan, H. N. Chapman, and S. Bajt, "Precise wavefront characterization of x-ray optical elements using a laboratory source," Rev. Sci. Instrum. **93**, 073704 (2022).
21. R. Conley, C. Liu, J. Qian, C. M. Kewish, A. T. Macrander, H. Yan, H. C. Kang, J. Maser, and G. B. Stephenson, "Wedged multilayer Laue lens," Rev. Sci. Instrum. **79**, 053104 (2008).
22. M. Prasciolu, A. Leontowich, J. Krzywinski, A. Andrejczuk, H. Chapman, and S. Bajt, "Fabrication of wedged multilayer Laue lenses," Opt. Mat. Express **5**, 748–755 (2015).
23. H. Yan, X. Huang, N. Bouet, J. Zhou, E. Nazaretski, and Y. S. Chu, "Achieving diffraction-limited nanometer-scale x-ray point focus with two crossed multilayer Laue lenses: alignment challenges," Opt. Express **25**, 25234–25242 (2017).
24. S. Bajt, M. Prasciolu, H. Fleckenstein, M. Domaracký, H. Chapman, A. Morgan, O. Yefanov, M. Messerschmidt, Y. Du, K. Murray, V. Mariani, M. Kuhn, S. Aplin, K. Pande, P. Villanueva-Perez, K. Stachnik, J. Chen, A. Andrejczuk, A. Meents, A. Burkhardt, D. Pennicard, X. Huang, H. Yan, E. Nazaretski, Y. Chu, and C. Hamm, "X-ray focusing with efficient high-na multilayer laue lenses," Light. Sci. Appl. **7**, 17162 (2018).
25. M. Fernández-Perea, M. J. Pivovaroff, R. Soufli, J. Alameda, P. Mirkarimi, M.-A. Descalle, S. L. Baker, T. McCarville, K. Ziock, D. Hornback, S. Romaine, R. Bruni, Z. Zhong, V. Honkimäki, E. Ziegler, F. E. Christensen, and A. C. Jakobsen, "Ultra-short-period WC/SiC multilayer coatings for x-ray applications," Nucl. Instrum. Meth. Phys. Res. A **710**, 114–119 (2013).
26. M. Prasciolu and S. Bajt, "On the properties of WC/SiC multilayers," Appl. Sci. **8**, 571 (2018).
27. H. N. Chapman, M. Prasciolu, K. T. Murray, J. L. Dresselhaus, and S. Bajt, "Analysis of x-ray multilayer Laue lenses made by masked deposition," Opt. Express **29**, 3097–3113 (2021).
28. T. Weitkamp, B. Nöhammer, A. Diaz, C. David, and E. Ziegler, "X-ray wavefront analysis and optics characterization with a grating interferometer," Appl. Phys. Lett. **86**, 054101 (2005).
29. M. Idir, P. Mercere, M. H. Modi, G. Dovillaire, X. Levecq, S. Bucourt, L. Escolano, and P. Sauvageot, "X-ray active mirror coupled with a hartmann wavefront sensor," Nucl. Instrum. Meth. Phys. Res. A **616**, 162–171 (2010).
30. S. Berujon, E. Ziegler, and P. Cloetens, "X-ray pulse wavefront metrology using speckle tracking," J. Synchr. Rad. **22**, 886–894 (2015).
31. F. Seiboth, M. Kahnt, M. Scholz, M. Seyrich, F. Wittwer, J. Garrevoet, G. Falkenberg, A. Schropp, and C. G. Schroer, "Quantitative characterization of aberrations in x-ray optics," in *Advances in X-Ray/EUV Optics and Components XI,* vol. 9963 (SPIE, 2016), pp. 88–95.
32. Y. Kayser, C. David, U. Flechsig, J. Krempasky, V. Schlott, and R. Abela, "X-ray grating interferometer for in situ and at-wavelength wavefront metrology," J. Synchr. Rad. **24**, 150–162 (2017).
33. J. Hagemann, A.-L. Robisch, M. Osterhoff, and T. Salditt, "Probe reconstruction for holographic x-ray imaging," J. Synchr. Rad. **24**, 498–505 (2017).
34. S. Matsuyama, T. Inoue, J. Yamada, J. Kim, H. Yumoto, Y. Inubushi, T. Osaka, I. Inoue, T. Koyama, K. Tono, H. Ohashi, M. Yabashi, T. Ishikawa, and K. Yamauchi, "Nanofocusing of x-ray free-electron laser using wavefront-corrected multilayer focusing mirrors," Sci. Rep. **8**, 17440 (2018).
35. J. Yamada, T. Inoue, N. Nakamura, T. Kameshima, K. Yamauchi, S. Matsuyama, and M. Yabashi, "X-ray single-grating interferometry for wavefront measurement and correction of hard x-ray nanofocusing mirrors," Sensors **20**, 7356 (2020).
36. S. Zhao, Y. Yang, Y. Shen, G. Cheng, Y. Wang, Q. Wang, L. Zhang, and K. Wang, "Optics metrology and at-wavelength wavefront characterization by a microfocus x-ray grating interferometer," Opt. Express **29**, 22704–22713 (2021).
37. A. J. Morgan, H. M. Quiney, S. Bajt, and H. N. Chapman, "Ptychographic x-ray speckle tracking," J. Appl. Cryst. **53**, 760–780 (2020).
38. A. J. Morgan, K. T. Murray, M. Prasciolu, H. Fleckenstein, O. Yefanov, P. Villanueva-Perez, V. Mariani, M. Domaracky, M. Kuhn, S. Aplin, I. Mohacsi, M. Messerschmidt, K. Stachnik, Y. Du, A. Burkhart, A. Meents, E. Nazaretski, H. Yan, X. Huang, Y. S. Chu, H. N. Chapman, and S. Bajt, "Ptychographic X-ray speckle tracking with multi-layer Laue lens systems," J. Appl. Cryst. **53**, 927–936 (2020).
39. A. J. Morgan, K. T. Murray, H. M. Quiney, S. Bajt, and H. N. Chapman, "speckle-tracking: a software suite for ptychographic x-ray speckle tracking," J. Appl. Cryst. **53**, 1603–1612 (2020).
40. N. Ivanov, J. L. Dresselhaus, J. Carnis, M. Domaracky, H. Fleckenstein, C. Li, T. Li, M. Prasciolu, O. Yefanov, W. Zhang, S. Bajt, and H. N. Chapman, "Robust ptychographic x-ray speckle tracking with multilayer Laue lenses," Opt. Express **30**, 25450–25473 (2022).
41. M. Born and E. Wolf, *Principles of optics: electromagnetic theory of propagation, interference and diffraction of light* (Elsevier, 2013).
42. B. Henke, P. Lee, T. Tanaka, R. Shimabukuro, and B. Fujikawa, "Low-energy x-ray interaction coefficients: Photoabsorption, scattering, and reflection: E= 100–2000 eV Z= 1–94," At. Dat. Nucl. Dat. Tab. **27**, 1–144 (1982).
43. F. Niesler and M. Hermatschweiler, "Two-photon polymerization—a versatile microfabrication tool: From maskless lithography to 3D printing," Laser Tech. J. **12**, 44–47 (2015).
44. "25x objective," https://support.nanoscribe.com/hc/en-gb/articles/360002482713-25x-Objective. Accessed: 2023-11-28.
45. J. Fischer and M. Wegener, "Three-dimensional optical laser lithography beyond the diffraction limit," Laser & Photonics Rev. **7**, 22–44 (2013).

46. D. Paganin, *Coherent X-ray optics*, 6 (Oxford University Press, USA, 2006).
47. W. Swantner and W. W. Chow, "Gram–Schmidt orthonormalization of Zernike polynomials for general aperture shapes," Appl. Opt. **33**, 1832–1837 (1994).
48. E. Muslimov, E. Hugot, W. Jahn, S. Vives, M. Ferrari, B. Chambion, D. Henry, and C. Gaschet, "Combining freeform optics and curved detectors for wide field imaging: a polynomial approach over squared aperture," Opt. Express **25**, 14598–14610 (2017).
49. R. J. Noll, "Zernike polynomials and atmospheric turbulence," J. Opt. Soc. Am. **66**, 207–211 (1976).
50. A. Kubec, M.-C. Zdora, U. T. Sanli, A. Diaz, J. Vila-Comamala, and C. David, "An achromatic x-ray lens," Nat. Comm. **13**, 1305 (2022).
51. U. T. Sanli, G. Rodgers, M.-C. Zdora, P. Qi, J. Garrevoet, K. V. Falch, B. Müller, C. David, and J. Vila-Comamala, "Apochromatic x-ray focusing," Light. Sci. Appl. **12**, 107 (2023).
52. M. D. Levenson, "Wavefront engineering for photolithography," Phys. Today **46**, 28–36 (1993).
53. C. G. Schroer, F. Seiboth, A. Schropp, S. Achilles, M. Seyrich, S. Patjens, M. E. Stuckelberger, J. Garrevoet, V. Galbierz, G. Falkenberg *et al.*, "Hard x-ray wavefront engineering for aberration correction and beam shaping," in *Advances in X-Ray/EUV Optics and Components XVII,* vol. 12240 (SPIE, 2022), pp. 163–170.
54. F. Seiboth, D. Brückner, M. Kahnt, M. Lyubomirskiy, F. Wittwer, D. Dzhigaev, T. Ullsperger, S. Nolte, F. Koch, C. David *et al.*, "Hard x-ray wavefront correction via refractive phase plates made by additive and subtractive fabrication techniques," J. Synchr. Rad. **27**, 1121–1130 (2020).
55. F. Seiboth, "Refractive phase plates for aberration correction and wavefront engineering," Synchr. Rad. News **35**, 43–48 (2022).